Research Square

Preprints are preliminary reports that have not undergone peer review.
They should not be considered conclusive, used to inform clinical practice,
or referenced by the media as validated information.

Towards strength-ductility synergy in bimodal-grained 7075Al matrix composites reinforced with high-content n-SiC by regulating coarse-grained components

Ruian Wang
Shanghai Jiao Tong University
Lichaoran Guan
Zhejiang University
Kan Liu
Shanghai Jiao Tong University
Yunpeng Cai
Shanghai Jiao Tong University
Yiwei Dong
Shanghai Jiao Tong University
Qiubao Ouyang
oyqb@sjtu.edu.cn

Shanghai Jiao Tong University
Yishi Su
Shanghai Jiao Tong University
Di Zhang
Shanghai Jiao Tong University

Research Article

Keywords:

Posted Date: November 5th, 2026

DOI: https://doi.org/10.21203/rs.3.rs-10995988/v1

License: This work is licensed under a Creative Commons Attribution 4.0 International License.
Read Full License

Additional Declarations: No competing interests reported.

Towards strength-ductility synergy in bimodal-grained 7075Al matrix composites reinforced with high-content n-SiC by regulating coarse-grained components

Ruian Wang [a], Lichaoran Guan [b,], Kan Liu [a,]*, Yunpeng Cai [a], Yiwei Dong [a], Qiubao Ouyang [a,]*, Yishi Su [a], Di Zhang [a]*

[a] State Key Laboratory of Metal Matrix Composites, School of Materials Science and Engineering, Shanghai Jiao Tong University, Shanghai, 200240, PR China

[b] State Key Laboratory of Fluid Power and Mechatronic Systems, School of Mechanical Engineering, Zhejiang University, Hangzhou, China

Corresponding author: e-mail: oyqb@sjtu.edu.cn; Tel: 86-21-34202524;

Fax: 86-21-34202749;

e-mail: liukan0204@sjtu.edu.cn; Tel: 86-21-34202524;

Fax: 86-21-34202749;

e-mail: guanlichaoran@163.com; Tel: 86-21-34202524;

Fax: 86-21-34202749;

Abstract

Owing to the inherent strength–ductility trade-off and complex changes in precipitation behavior, the design of 7xxxAl composites with high n-SiC content has long been a formidable challenge. Here, we fabricated a bimodal n-SiC/7075Al composite in powder metallurgy route and investigated the role of coarse-grained (CG) microstructures in mechanical responses. The spatially alternate arrangement of ultrafine-grained (UFG) zones with high-content (10 wt%) n-SiC and CG zones without n-SiC delivers superior mechanical properties: yield strength (YS) of 538.4 MPa, ultimate tensile strength (UTS) of 662.0 MPa, elongation (El) of 5.7% and a strain

hardening exponent of 0.078. Compared with 7075Al, the suppressed intragranular nanoprecipitates by dispersive n-SiC/Al interfaces facilitate the hetero-deformation-induced (HDI) stress as dominant strengthening contribution rather than Orowan mechanism. The improved ductility is attributed to the synergy of both intrinsic and extrinsic toughening mechanisms. The former origins from the enhanced HDI strain hardening capacity by means of strain gradients and nanoprecipitates; while the latter derives from the delocalized nucleation and growth of microcracks.

1. Introduction

As a precipitation-strengthening alloy, 7075Al derives its exceptionally high strength from Orowan strengthening induced by the high-density GPII zones and η′ phases that precipitate after T6 heat treatment, maintaining a coherent/semi-coherent relationship with the matrix [1-4]. Currently, 7075Al alloy finds extensive application in aerospace, weaponry, and rail transport sectors [5, 6]. To accommodate more demanding and extreme service conditions, incorporating ceramic particles (SiC, TiB_2, B_4C, Al_2O_3) into metals can effectively enhance the material's strength, stiffness, hardness, and wear resistance [7-10].

Given that conventional micron or hybrid particle reinforced 7xxxAl matrix composites exhibit simultaneous loss of both strength and ductility [10, 11], the incorporation of nanoparticles theoretically offers superior properties. However, incorporating high-content nano-reinforcements into precipitation-strengthened alloys not only poses the challenge of agglomeration arising from their high surface energy, but can also disrupt the aging precipitation sequence owing to the presence of high-density interfaces and defects, ultimately leading to a pronounced loss of ductility.[12-14]. Therefore, it is imperative to develop effective strategies that enhance the strength of 7xxxAl matrix composites while preserving their ductility.

Heterogeneous grain structure design actively constructs non-uniform microstructures, combining regions with differing mechanical properties in a specific manner. This approach effectively utilizes strain gradient and HDI strengthening to achieve simultaneous enhancement of strength and ductility. Liu et al. [15] successfully

fabricated a bimodal-grained TiB_2/Al-Zn-Mg-Cu composite, which achieved a YS of 774 MPa, an UTS of 813 MPa, while maintaining an El of 6%. Research by Guan et al. [16] has also demonstrated that SiC/2024Al composites based on a bimodal grain structure achieve simultaneous enhancement of strength and ductility. This is facilitated by the combined effects of HDI strain hardening and increased dislocation accumulation capacity, coupled with the crack passivation effect exerted by CG zone. Liu et al. [17] prepared m-&n-SiCp/Al composites with a bimodal grain structure by adjusting strain energy input and introducing n-SiC. Its toughness was enhanced by 267% and 175% respectively compared to homogeneous FG and UFG structured composites. Given the inherently low ductility of 7xxxAl alloys and the strength-ductility inversion dilemma faced by conventional composites, a bimodal grain structure has been incorporated into the composite material to achieve simultaneous enhancement of both strength and ductility.

To this end, a bimodal-grained n-SiC/7075Al composite was fabricated via high-energy ball milling and vacuum hot-pressing sintering. The precipitation behavior and deformation mechanisms in CG and UFG zones were systematically characterized. By combining tensile and LUR tests, the influence of the bimodal grain structure on strength and ductility was clarified, and the contributions of the dominant strengthening mechanisms were quantitatively evaluated.

2. Experiments

2.1 Material preparation

The raw materials required for sample preparation, namely 7075Al powder and n-SiC powder, were supplied by TJO Industry & Trade Co., Ltd. (Hunan, China) and Aladdin Industrial Co. LLC respectively. The alloy composition of 7075Al powder is shown in Table 1.

Table1. Chemical compositions of 7075Al powders

Components	Al	Zn	Mg	Cu	Fe	Mn	Cr	Si
Contents/ wt%	bal.	5.218	2.180	1.464	0.251	0.136	0.189	0.152

The 7075Al powders were mixed with n-SiC powders and subjected to ball milling under an argon atmosphere of 1 atm with a ball-to-powder ratio of 20:1, using a total of 75 g of mixed powders. Two types of milled powders were produced: high-speed ball-milled (HSB) powders, containing 10 wt% n-SiC, milled at 250 rpm for 4 hours; and low-speed ball-milled (LSB) powders, with 3 wt% n-SiC, milled at 100 rpm for 8 hours. Heterostructured composite powders were subsequently prepared by blending the HSB powder with either LSB powder or 7075Al powder, with a total mass of 70 g for each composite mixture. The blending mass ratios were set as HSB: LSB = 3:1 for HSB+LSB, and HSB:7075 = 3:1 for HSB+7075. The powder blending process was carried out in a drum mixer operated at a rotational speed of 120 rpm, using ZrO_2 balls with a ball-to-powder ratio of 5:1.

The composite powders were loaded into a steel mold with a diameter of 36 mm and consolidated via hot-press sintering. The process was conducted at a temperature of 540 °C for 1 hour, with a uniaxial pressure of 300 MPa applied during the final 10 min. Throughout sintering, a vacuum level of 10^{-3} Pa was sustained. The sintered specimens were extruded at 400 °C using an extrusion ratio of 16:1. The extrusion rods were solution treated at 470 °C for 1 hour and quenched in cold water. Subsequently, artificial aging was performed at 120 °C for 24 hours, followed by air cooling. The flowchart for material preparation is shown in Fig. 1.

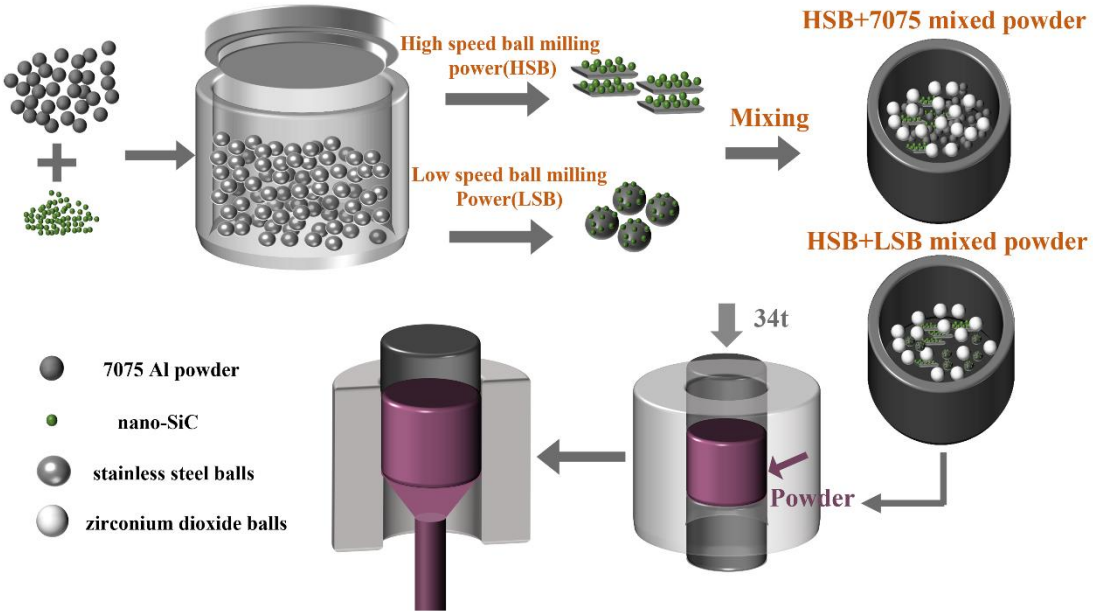


Fig. 1. The fabrication processes of bimodal structured composites.

2.2 Microstructural characterizations and mechanical tests

Field emission scanning electron microscopy (FE-SEM, MIRA3, TESCAN), electron backscatter diffraction (EBSD, Sigma30, ZEISS), and field emission transmission electron microscopy (FE-TEM, Talos F200X G2, Thermo Scientific) were employed to characterize the microstructures (grains and precipitates). The EBSD results were analyzed using AZtec Crystal software to generate inverse pole figure (IPF) maps, pole figure (PF) maps, grain orientation spread (GOS) maps, kernel average misorientation (KAM) maps, and grain size distribution plots. Specimens for EBSD experiments were prepared using a triple ion beam cutter (EM TIC 3X, Leica). Thin sections with a diameter of 3 mm and thickness below 20 μm were thinned using an ion thinning apparatus (PIPS695, Gatan) to meet TEM requirements. X-ray diffraction (XRD, D8 ADVANCE Da Vinci, Bruker) with Cu Kα radiation was employed for phase identification of powders and bulk specimens. Three-dimensional imaging of the spatial distribution of cracks on the tensile fracture surface was performed using high-resolution CT (Xradia 620 Versa, Carl Zeiss).

Quasi-static tensile tests and loading-unloading-reloading tests (LUR) were conducted on a universal testing machine (Instron 3344) at a tensile rate of 0.3 mm/min. The extensometer gauge length was set to 10 mm. Rectangular tensile specimens featured a gauge length of 15 mm, a width of 2 mm, and a thickness of 1.2 mm. The LUR tests employed a cyclic strain amplitude of 0.5%.

3. Results

3.1 Microstructural characterization results

Fig. 2 presents the SEM and XRD results of 7075Al, HSB and LSB powders. The as-received 7075Al powder exhibits a nearly spherical morphology with an average particle size of 13.6 μm (Fig. 2 (a)). The LSB powder (Fig. 2(b)) maintains its structural integrity without significant flaking after low-speed ball milling, while the n-SiC is uniformly dispersed to cover its surface. Following high-speed ball milling, the composite powder undergoes flaking before re-aggregating and bonding to form larger

cold-welded particles (Fig. 2(c)). Both the surface layer and core of these cold-welded particles exhibit a uniform distribution of n-SiC. The XRD results for both HSB and LSB powders clearly show distinct n-SiC diffraction peaks. In addition, the broadened Al (111) peak observed in HSB powders compared with 7075 and LSB powders suggests an increased defect density and strain energy.

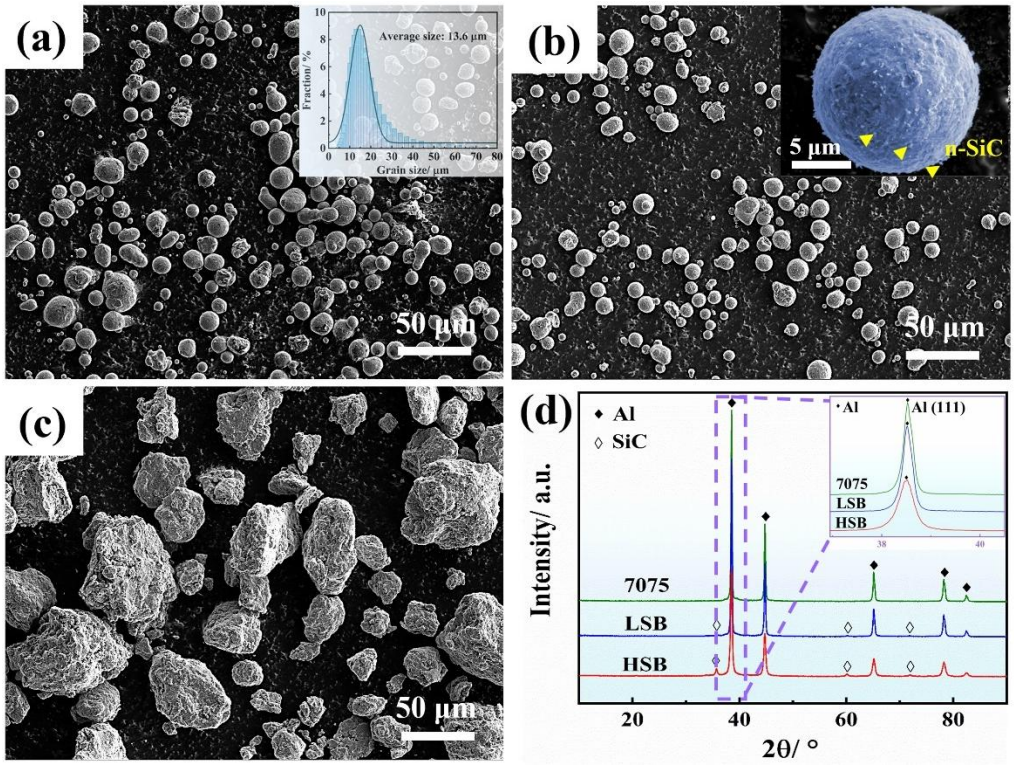


Fig. 2. SEM images of: (a) 7075Al powders, with inset is particle size distribution, (b) LSB powders, with inset shows a detailed view of dispersed n-SiC adhering to the surface of 7075Al powder. (c) HSB powders, (d) XRD patterns of different powders, with inset is a magnified view of the Al (111) peak.

Fig. 3 presents the microstructures of composites and 7075Al. Both HSB+LSB and HSB+7075 exhibit pronounced heterogeneous grain structures (Fig. 3(a, b, d, e)). The band-like CG and UFG zones are spatially alternated to form a high density of domain interfaces. The n-SiC is selectively enriched in UFG zones, while the large grains in the CG zone are elongated along the extrusion direction. As shown in Fig. 3(c, f), a small number of rod-like precipitates are sporadically distributed within the UFG regions. These coarsened precipitates have average dimensions of approximately 200 nm in length and 20 nm in width. For comparison, Fig. 3(g) shows the bright-field STEM (BF-STEM) image of 7075Al, where Al grains are similarly elongated along the

extrusion direction. The XRD results presented in Fig. 3(i) confirm the presence of the (222) diffraction peak of $MgZn_2$ [18, 19, 21].

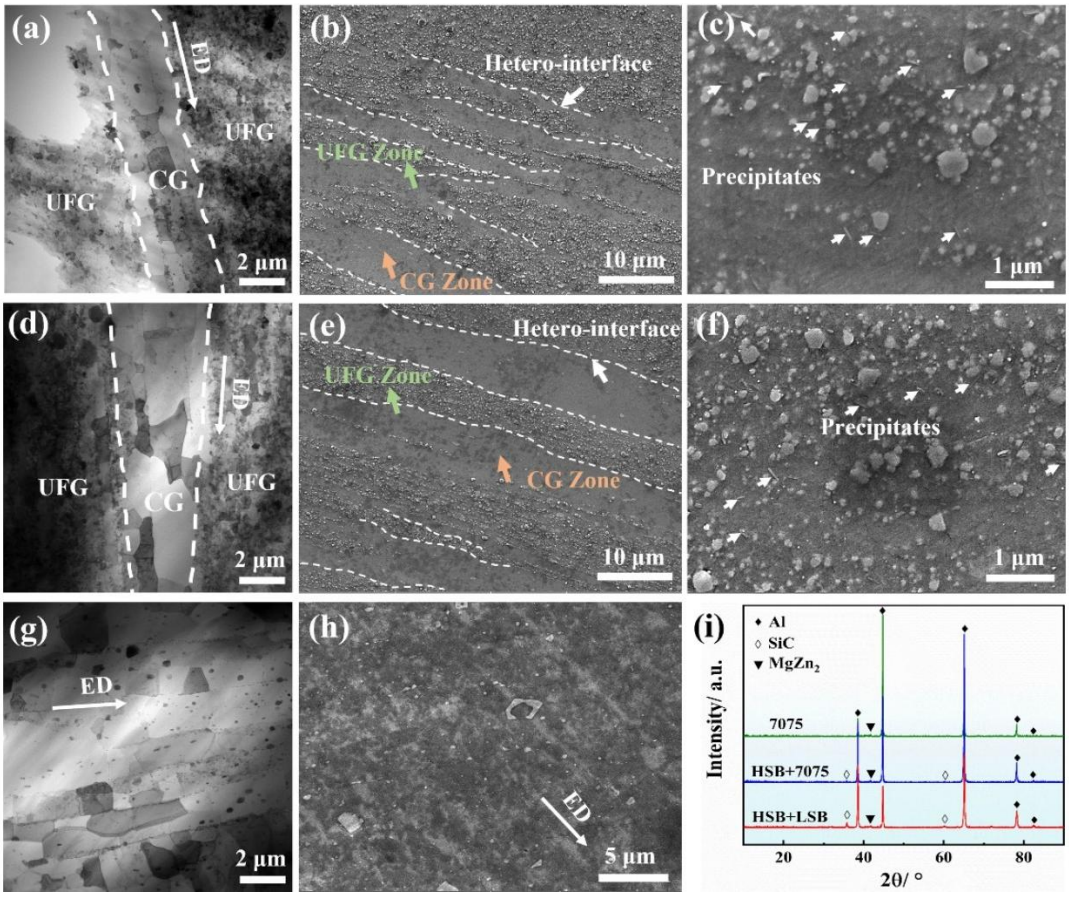


Fig. 3. TEM BF-STEM image of samples after aging: (a) HSB+LSB, (d) HSB+7075, (g) 7075Al; Low magnification SEM image of samples: (b) HSB+LSB, (e) HSB+7075, (h) 7075; High magnification SEM image of samples: (c) HSB+LSB, (f) HSB+7075, (i) XRD patterns.

Fig. 4 presents the EBSD results of composites and 7075Al. Given that 7075Al possesses an FCC crystal structure with a {111}⟨110⟩ slip system, the ⟨111⟩ axis is preferentially parallel to the extrusion direction, as observed in the CG zones of HSB+LSB and HSB+7075 as well as in most grains of the 7075Al (Fig. 4(a_1-a_3)) [17], which is widely recognized as the {112}⟨111⟩ copper texture developed during extrusion deformation. The high stacking fault energy inherent to aluminum promotes dynamic recovery during thermo mechanical processing, e.g., hot extrusion, which is further enhanced in the presence of a high content of n-SiC, as evidenced in the UFG zones of composites and certain areas of 7075Al (Fig. 4(c_1-c_3)). The lower GOS values, specifically those “cold spots” representing GOS < 2°, are indicative of a greater extent

of recrystallization. As shown in Fig. 4(e_1-e_3), the ⟨111⟩ texture strengths of HSB+LSB, HSB+7075 and 7075Al are 16.55, 9.47, and 24.06, respectively. The reduction in texture strength of the composites compared to the alloy correlates with the high degree of recrystallization within their UFG zones [22].

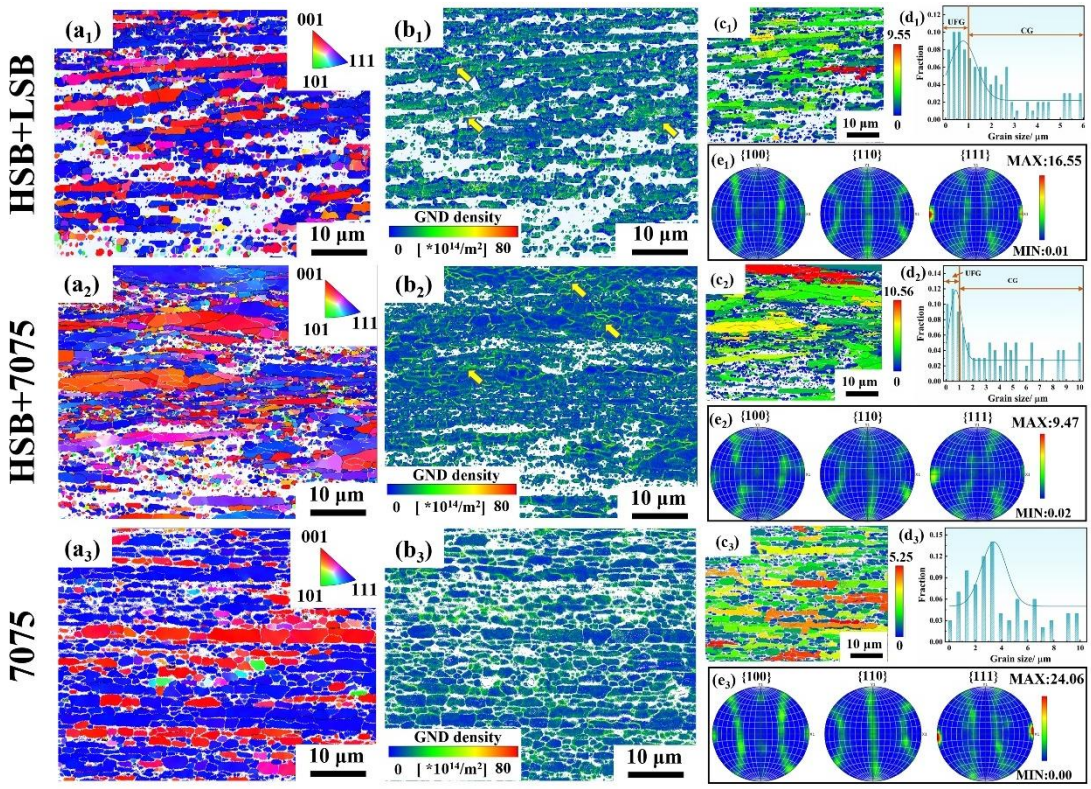


Fig. 4. EBSD results of HSB+LSB, HSB+7075 and 7075Al: (a_1-a_3) IPF, (b_1-b_3) KAM figure, (c_1-c_3) GOS figure, (d_1-d_3) grain size distribution figure, (e_1-e_3) PF.

High density dislocations in composites are predominantly localized at CG boundaries and heterogeneous interfaces (Fig. 4(b_1, b_2)). During hot extrusion, the differential deformation capacities between hard (UFG) and soft (CG) zones prompt the accumulation of geometrically necessary dislocations (GNDs) at these heterogeneous interfaces, thereby accommodating the resulting strain gradient. The grain size distribution diagram of the composites (Fig. 4(d_1, d_2)) also exhibits a pronounced bimodal grain structure. In HSB+LSB, CG and UFG exhibited average grain sizes of 3.51 μm and 309 nm, respectively. This contrasts with HSB+7075, which showed corresponding values of 5.71 μm and 235 nm. Given that the CG zone of the HSB+7075 is derived from unmilled 7075 powder and lacks the pinning effect of n-SiC at grain boundaries, its average grain size is therefore significantly larger than that

in HSB+LSB. The average grain size of the 7075Al was 8.25 μm. Further details regarding the EBSD experimental results are presented in Table 2.

Table 2. Statistical results of 7075Al and n-SiC/7075Al composites from EBSD.

	Average grain size/μm		Fraction of GB/%		Fraction of grain with GOS<2°	GND density/10^{14}·m^{-2}	Maximum texture intensity
	CG	UFG	HAGBs	LAGBs			
HSB+LSB	3.51	0.309	86.9	13.1	55.5%	12.9	16.55
HSB+7075	5.71	0.235	78.7	21.3	39.8%	16.2	9.47
7075	8.25		71.8	28.2	53.5%	13.0	24.06

Fig. 5 shows the TEM characterization of the CG zone in HSB+LSB. As shown in Fig. 5(a) and the corresponding EDS mappings (Fig. 5(a_1-a_4)), n-SiC are distributed both within the CG and along grain boundaries. This observation is attributed to the partial migration of n-SiC originally covering the surface of LSB powders into grain interiors during hot extrusion. Moreover, the spatial distributions of Mg and Zn are highly correlated with those of n-SiC, indicating that precipitates preferentially nucleate and grow in regions adjacent to these reinforcing nanoparticles. Fig. 5(b) shows an HRTEM image of region b in Fig. 5(a), demonstrating defect-free interfacial bonding between n-SiC and the Al matrix. Fig. 5(b_1, b_2) present the fast Fourier transform (FFT) patterns of Al $[0\bar{1}1]$ and SiC [100] with long period stacking ordered structure. Fig. 5(c) shows a dark-field STEM (DF-STEM) image of grain boundary precipitates (GBPs). The average length and width of the GBPs are measured to be 18.03 nm and 8.98 nm, respectively (Fig. 5(c_1, c_2)); they are likely the $Mg(Zn, Cu, Al)_2$ phase or the η phase [7, 15, 20]. Fig. 5(d) shows a typical HRTEM image of a triple-phase interface between the Al matrix, a precipitate, and n-SiC. The FFT patterns taken from the regions marked by the yellow boxes (Fig. 5(d)) confirm that the precipitate is the η′ phase with a hexagonal structure, maintaining an $[10\bar{1}0]$ η′//Al $[0\bar{1}1]$ orientation relationship with the Al matrix [23-25]. Fig. 5(e) presents the DF-STEM diagram of η′ phases in the CG interior, showing that they precipitated along dislocations with specific orientations (i.e., $(\bar{1}1\bar{1})$

and ($\bar{1}\bar{1}1$) planes in [$0\bar{1}1$] Al zone axis) [26-29], rather than being randomly distributed as commonly reported in 7xxxAl alloys. HRTEM and FFT images of the precipitates are shown in Fig. 5(f, f_1, f_2), confirming that the two precipitates correspond to the η′ phase and GPII zone, respectively [30, 31]. Statistical analysis of their average length and width yields values of 11.73 nm and 2.13 nm, respectively (Fig. 5(f_3, f_4)).

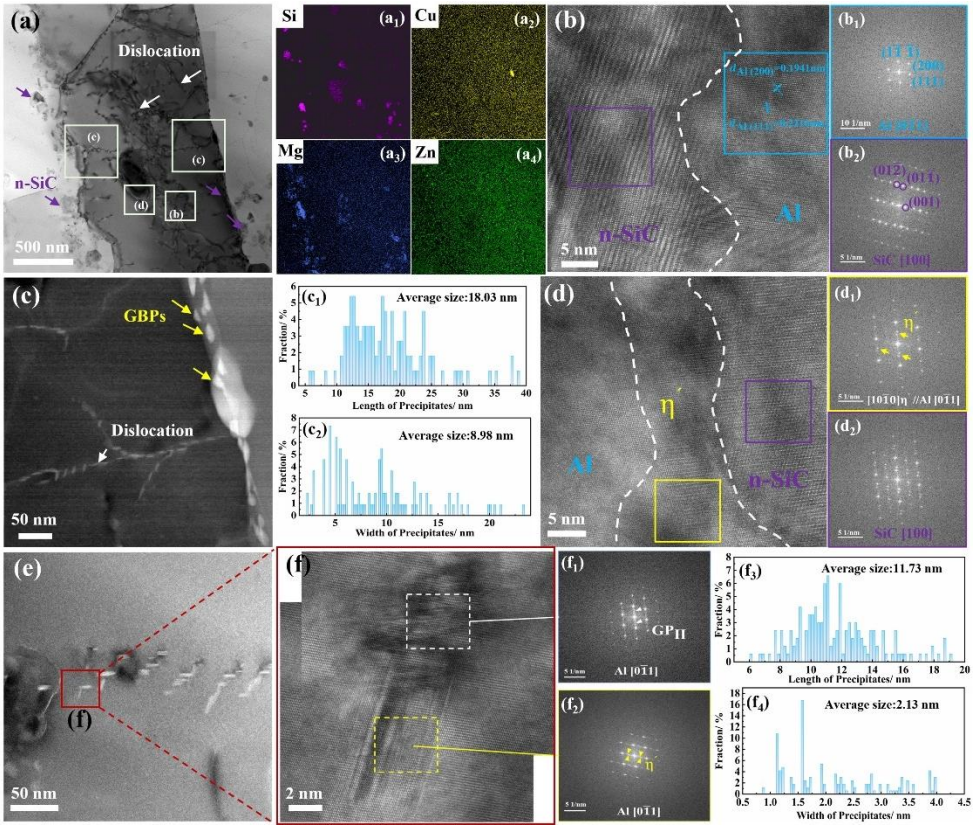


Fig. 5. TEM microstructure of CG zone in HSB+LSB: (a, a_1-a_4) BF-STEM image and corresponding EDS mappings, (b, b_1, b_2) HRTEM image of region b in figure a and corresponding FFT image of Al[$0\bar{1}1$] and SiC[100], (c, c_1, c_2) DF-STEM image of region c in figure a and histogram of GBPs size, (d, d_1,d_2) HRTEM image of region d in figure a and corresponding FFT image of η′ and SiC[100], (e) DF-STEM of region e in figure a, (f) HRTEM image of region f in figure e, (f_1, f_2) corresponding FFT image of Al[$0\bar{1}1$], (f_3, f_4) histogram of intragranular precipitate size.

Fig. 6(a) shows the BF-STEM image and corresponding EDS mappings (Fig. 6(a_1-a_4)) of HSB+7075. In contrast to HSB+LSB, no n-SiC are present within the CG zones, and Mg, Zn, and Cu are uniformly distributed without segregation near nanodispersoids. Fig. 6(b) presents a BF-STEM image of region b in Fig. 6(a), revealing active dislocation forest hardening with entanglements within the CG interior, further

enhanced by the elevated dislocation density near the CG/UFG domain interface. Note that no significant defect-dependent precipitation behavior similar to that observed in HSB+LSB is found in the CG of HSB+7075; instead, the nanoprecipitates are uniformly distributed rather than growing along dislocations or interfaces (Fig. 6(c)). As shown in Fig. 6(d), HRTEM and FFT images reveal η' phase growing on the $(1\bar{1}1)$ plane, viewed along the $[\bar{1}\bar{1}0]$ Al zone axis; these precipitates exhibit average lengths and widths of 10.72 nm and 1.59 nm, respectively (Fig. 6(d_1, d_2)). Fig. 6(e, e_1-e_4) present the BF-STEM image of a representative UFG in the HSB+7075 and the corresponding EDS maps. The n-SiC, which were subjected to intense shear during high-speed ball milling, are distributed both at UFG boundaries and interiors, while Mg and Zn are segregated near crystal defects such as n-SiC/Al interfaces and grain boundaries. Additionally, intragranular precipitates (IGPs) with an average diameter of 12.44 nm are also observed within the UFG (Fig. 6(f)).

Fig. 7(a) shows a BF-STEM micrograph of the 7075Al for comparison. Coarse precipitates form at grain boundaries due to the enrichment of Mg, Zn, and Cu, leading to solute depletion adjacent to the boundaries and the formation of precipitate-free zones (PFZs) [1, 15, 32]. The average width of the PFZs is measured to be 53.94 nm. Within the grain interiors, a high density of precipitates is observed, with average dimensions of 7.90 nm in length and 2.34 nm in width (Fig. 7(b_1, b_2)). HRTEM and FFT images (Fig. 7(c, d, e)) of these precipitates reveal the presence of both the η' phase and the η phase in 7075Al.

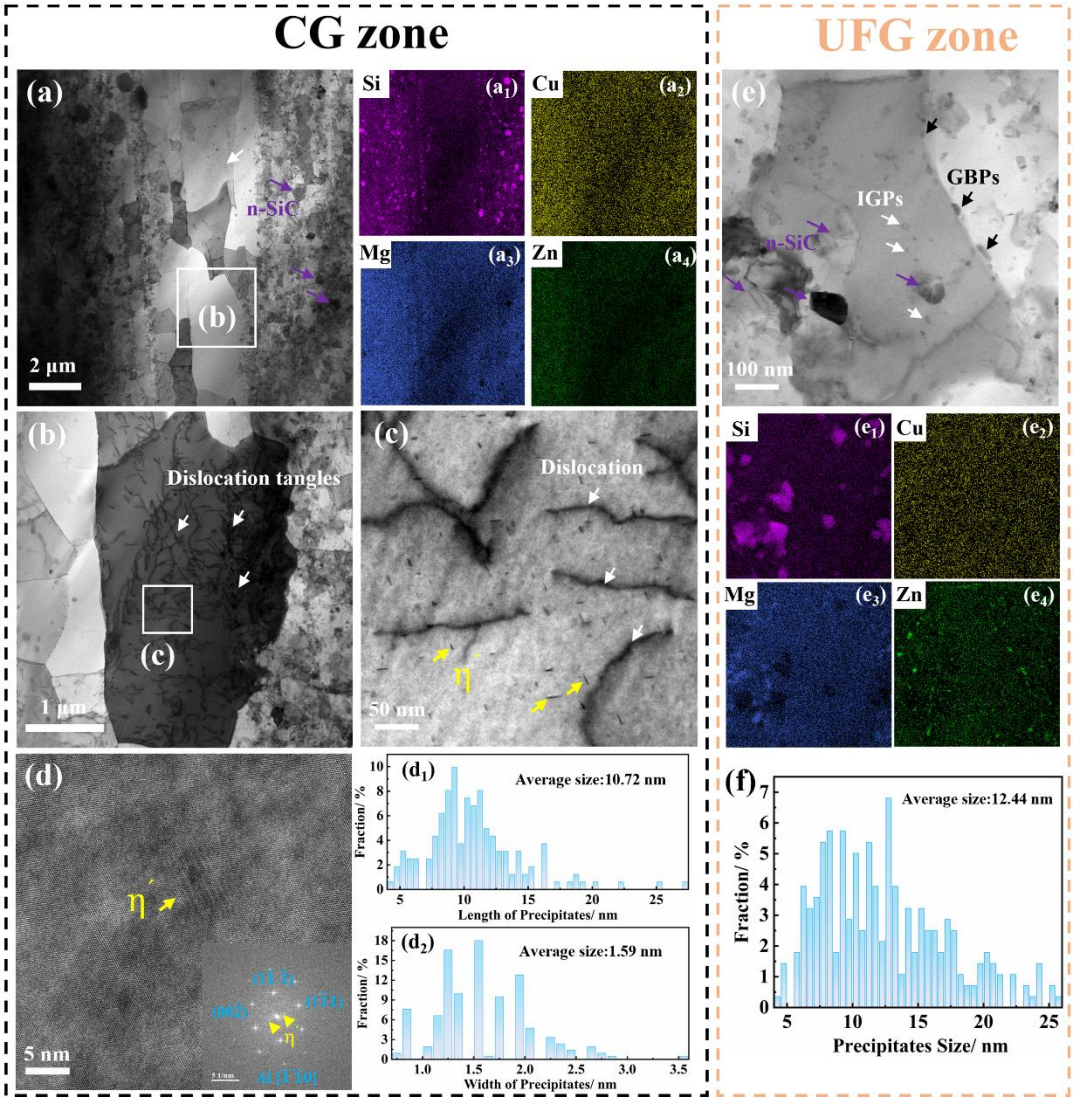


Fig. 6. TEM microstructure of CG zone in HSB+7075: (a, a_1-a_4) BF-STEM image and corresponding EDS mappings, (b) DF-STEM image of region b in figure a, (c) DF-STEM image of region c in figure b, (d, d_1, d_2) HRTEM image of η′ in figure c (inset shows the FFT image of Al [$\bar{1}\bar{1}0$]) and histogram of intragranular precipitate size, TEM microstructure of the UFG zones in HSB+7075: (e, e_1-e_4) BF-STEM image and corresponding EDS mappings, (f) histogram of precipitate diameter.

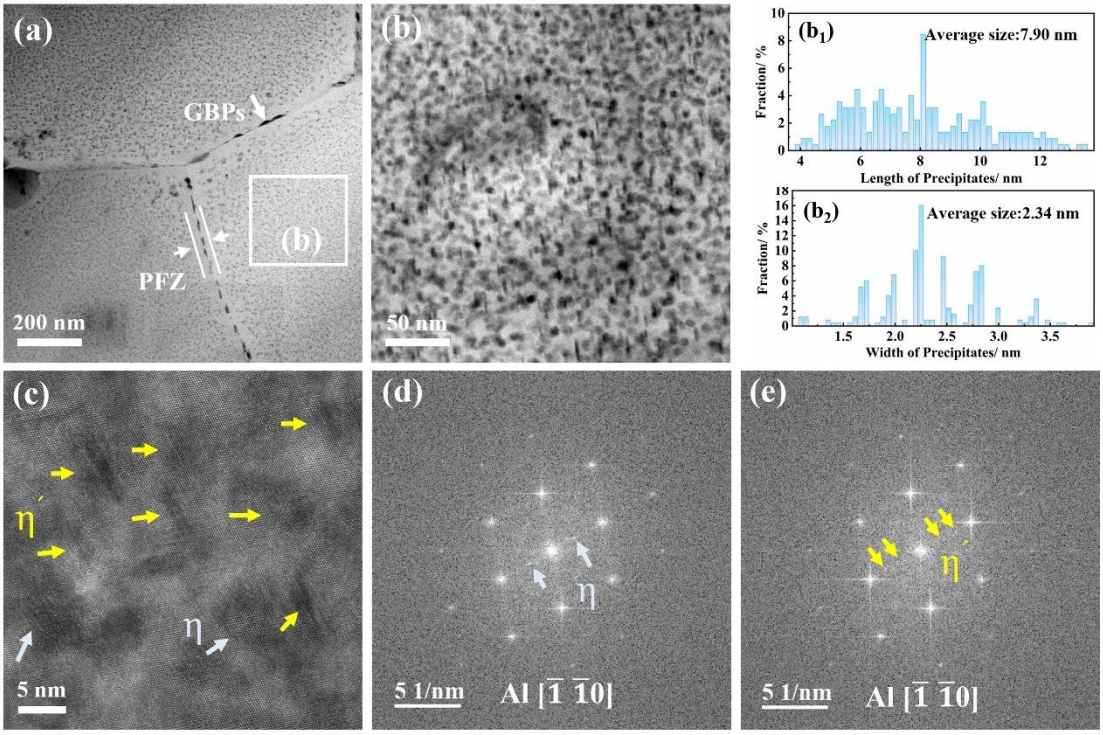


Fig. 7. TEM microstructure of 7075Al: (a) BF-STEM image, (b, b_1, b_2) BF-STEM image of region b in figure a and histogram of precipitate size, (c, d, e) HRTEM and FFT image of precipitate.

3.2 Mechanical test results

Fig. 8(a) shows the engineering stress-strain curves of HSB+LSB, HSB+7075 and 7075Al. The detailed tensile properties are presented in Table 3. Due to the dispersed high-stiffness n-SiC, the elastic modulus of the composites exceeds 82 GPa, representing a maximum increase of 23% relative to 7075Al. Notably, unlike the linear stress-strain response of homogeneous 7075Al, the slope of the stress-strain curve for HSB+7075 begins to decrease when the stress reaches 538.4 MPa, even though a macroscopic plastic flow has not yet occurred. Such a premature yielding, i.e., conditional yielding $\sigma_{0.2}$, is mainly facilitated by the localized plastic deformation initiated preferentially in CG zones, denoted as YS_I, which is comparable to that (532.7 MPa) of 7075Al. Then, as the stress further increases to 604.4 MPa, the slope drops sharply to a minimum, suggesting that slip systems are widely activated, including those in UFG zones, and plastic flow initiates. The observed overall yielding point, denoted as YS_{II}, is 13% higher than YS_I of 7075Al. For HSB+LSB, the CG is dispersion-strengthened by n-SiC, giving rise to a higher YS_I (547.9 MPa) than that of

HSB+7075; however, YS_{II} is nearly identical, which is likely governed by the volumetrically dominant UFG zones. Thus, HSB+7075 exhibits superior comprehensive mechanical properties, e.g., 662.0 MPa in UTS and 5.7% in El to fracture, with the former being nearly identical to HSB+LSB, while the latter is 20% higher.

Table 3. Mechanical properties of 7075Al and n-SiC/7075Al composites.

Sample	UTS/MPa	YS_I/MPa	YS_{II}/MPa	El/%	E/GPa	UTS-YS_I/MPa
HSB+LSB	663.7±3.9	547.9±3.9	605.0±7.5	4.8±0.8	86.6±0.3	115.8
HSB+7075	662.0±2.3	538.4±2.2	604.4±11.4	5.7±0.5	82.6±0.4	123.6
7075	591.6±5.6	532.7±0.4	/	8.6±2.4	70.2±1.0	58.8

Note that compared with 7075Al, composites exhibit a much higher UTS-YS_I value, and especially that of HSB+7075 reaches a maximum of 123.6 MPa. Such larger strain hardening interval implies an enhanced strain hardening capacity. Fig. 8(b) shows the strain hardening rate (SHR, $\psi=ds/de$, where s and e denote true stress and true strain, respectively) curves for composites and 7075Al. They all exhibit a three-stage strain hardening behavior, i.e., the strain hardening rate first drops to a minimum upon the termination of elastic stage, then rapidly climbs to a peak with plastic flow lasting, and finally decreases gradually until it intersects the true stress-strain curve. The Considère criterion attributes the onset of necking and plastic instability to the condition $s=ds/de$, implying that an improved strain hardening rate can not only strengthen the flow stress but also increase the uniform El. A higher peak strain hardening rate and a more gradual post-peak decay are observed in HSB+7075, compared with 7075Al, indicating an enhanced strain hardening capacity, which can be quantified by the strain hardening exponent n. Based on the power law $\sigma_p=K\varepsilon_p^n$ (where σ_p and ε_p represent the plastic stress and strain, respectively) that describes the mechanical responses during plastic deformation, the n values for 7075Al and HSB+7075 are determined by curve fitting to be 0.058 and 0.078, respectively. The n value of 7075Al is consistent with the reported

range of 0.03-0.08; while that observed in HSB+7075 is unusual, since the incorporation of nanodispersoids generally reduces the *n* value due to limited ductility and dislocation annihilation at extra particle interfaces. Although the highest peak strain hardening rate is found in HSB+LSB, the subsequent rapid decay results in the lowest uniform El; its strain hardening capacity is slightly inferior to that of HSB+7075, with an *n* value of 0.070.

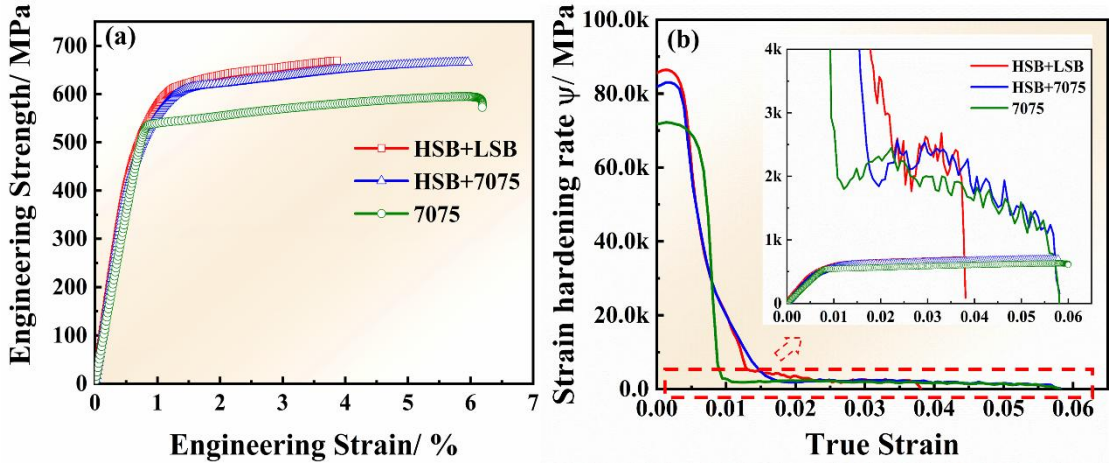


Fig. 8. Tensile test results for different samples: (a) engineering stress-strain curve, (b) strain hardening rate curve.

Fig. 9(a, b) show the fracture surface morphologies of HSB+LSB and HSB+7075, respectively. The CG zones exhibit large, deep, and well-defined dimples accompanied by pronounced tearing ridges, indicative of extensive plastic flow and void growth prior to final fracture. By comparison, the UFG zones display a high density of fine and shallow dimples, resulting in a comparatively smoother fracture surface. Notably, n-SiC embedded at the bottom of the UFG dimples act as dominant microvoid nucleation sites due to elastic and thermal mismatch with the Al matrix. The tensile fracture surface of 7075Al exhibits elongated ductile dimples oriented at 45° to the tensile direction (Fig. 9(c)), representing a characteristic microstructural feature of ductile shear fracture under tensile loading. Additionally, larger $Al_6(Fe, Mn)$ phases appear at the bottom of the ductile dimples. A low-energy intergranular fracture can be triggered by the rapid coalescence of microvoids along grain boundaries, which originate from the debonding of coarse intermetallic particles at the boundaries. This mechanism is observed on the tear ridges in both the composite and the alloy (marked in the Fig. 9 with a red circle).

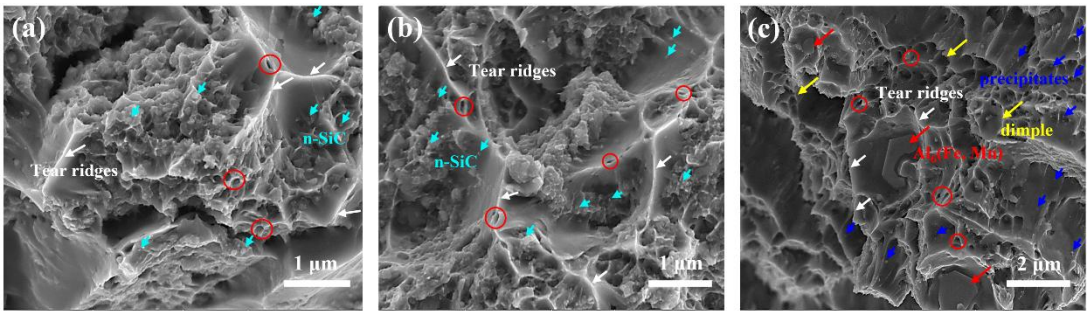


Fig. 9. SEM image of the tensile fracture surface: (a)HSB+LSB, (b)HSB+7075, (c)7075Al.

4. Discussions

4.1 Heterogeneous microstructures induced toughening behaviors

According to the Considère criterion, necking instability and rapid failure occur once the strain hardening rate drops to flow stress, i.e., $\psi = ds/de = s$, as shown in Fig. 8(b). Therefore, HSB+7075 exhibits comparable UTS and higher uniform El by virtue of stronger strain hardening capacity, although the YS is slightly lower than that of HSB+LSB.

It is widely acknowledged that HDI hardening constitutes the microstructural basis for the strain-hardening response in heterostructured materials [16, 33, 34]. To elucidate the origins of variations in strain hardening and intrinsic toughening behaviors, LUR tests (Fig. 10(a)) were conducted to track the dynamic evolutions of microstructure dependent HDI stress during uniaxial tensile deformation. Compared with 7075Al, HSB+LSB and HSB+7075 exhibit notably larger hysteresis loops, which manifests as the pre-yield precursors of Bauschinger effect, indicating long-range HDI stress induced by microstructural heterogeneities. By analyzing each individual unloading-reloading event (Fig. 10(b)) following the methodology summarized by Wu [35]:

$$\sigma_{HDI} = \frac{\sigma_r + \sigma_u}{2} \tag{1}$$

$$\sigma_{eff} = \sigma_{flow} - \sigma_{HDI} \tag{2}$$

The evolutions of flow stress (σ_{flow}), effective stress (σ_{eff}) and HDI stress (σ_{HDI}) as a function of true strain are quantified in Fig. 10(c-e), respectively.

Fig. 10(d) presents the evolution of HDI stress. For both HSB+LSB and 7075Al, the HDI stress increasing monotonically with strain, approaches a near-saturation state

at the terminal plastic stage, attributable to the GND accumulation driven by strain gradients. Specifically, continued plastic deformation progressively alleviates the mechanical incompatibility between distinct microstructural units, thereby weakening the strain gradients in the interfacial regions. The suppressed GND emission decelerates the growth rate of HDI stress, which aligns with the precipitous decline in SHR during the late plastic stage. The higher HDI stress in HSB+LSB relative to 7075Al originates from UFG/CG gradient grain structure and the dispersed n-SiC/Al interfaces. Notably, despite exhibiting a consistently lower flow stress compared with HSB+LSB, HSB+7075 manifests a higher HDI stress level, and furthermore, a distinct advantage in HDI stress growth rate, enabling a climb even at the terminal plasticity stage. Through a detailed comparative analysis of the microstructural differences between HSB+LSB and HSB+7075, such a sustained HDI strain hardening capability can be ascribed to two factors: 1) In contrast to the other counterparts, the UFG components incorporating a high content of n-SiC via HSB process, alongside the n-SiC-free CG structure, engender a substantial strain incompatibility that maximizes the strain gradients at UFG/CG hetero-interfaces; 2) It is precisely due to the lack of n-SiC in CG zones of HSB+7075 that a higher density of $MgZn_2$ nanoprecipitates are retained compared to HSB+LSB (the underlying mechanisms are discussed in Section 4.2). The copious intragranular $MgZn_2$/Al interfaces can improve GND multiplication through strain partitioning, with their contribution even significantly surpassing that of n-SiC/Al interfaces. EBSD analysis of CG subset (Fig. S3 and Table S1) confirms a more uniform dislocation substructure within CG zones after deformation, indicating enhanced GNDs stored. Consequently, the superior HDI kinematic hardening governs the strain hardening of HSB+7075, conferring upon it the highest strain hardening exponent and uniform elongation among the three samples [36, 37].

Besides, Fig. 10(e) shows the effective stress curves. Unlike long-range HDI stress, effective stress, originating from the forest dislocation cutting and dislocation-lattice interactions, represents the isotropic resistance to slip. Relative to 7075Al, HSB+LSB and HSB+7075 show a sharper increase in effective stress at the onset and a steeper decrease in the late plasticity stage. This could be rationalized by: 1) The rapid

multiplication of GND forests upon UFG/CG hetero-interfaces and their frequent intersection with gliding dislocations in the early plastic stage; 2) The combined effect of dynamic recovery of mobile dislocations and dislocations absorbed into high-density grain boundaries of UFG zones in the terminal plastic stage, which weakens the dislocation interactions[39, 40].

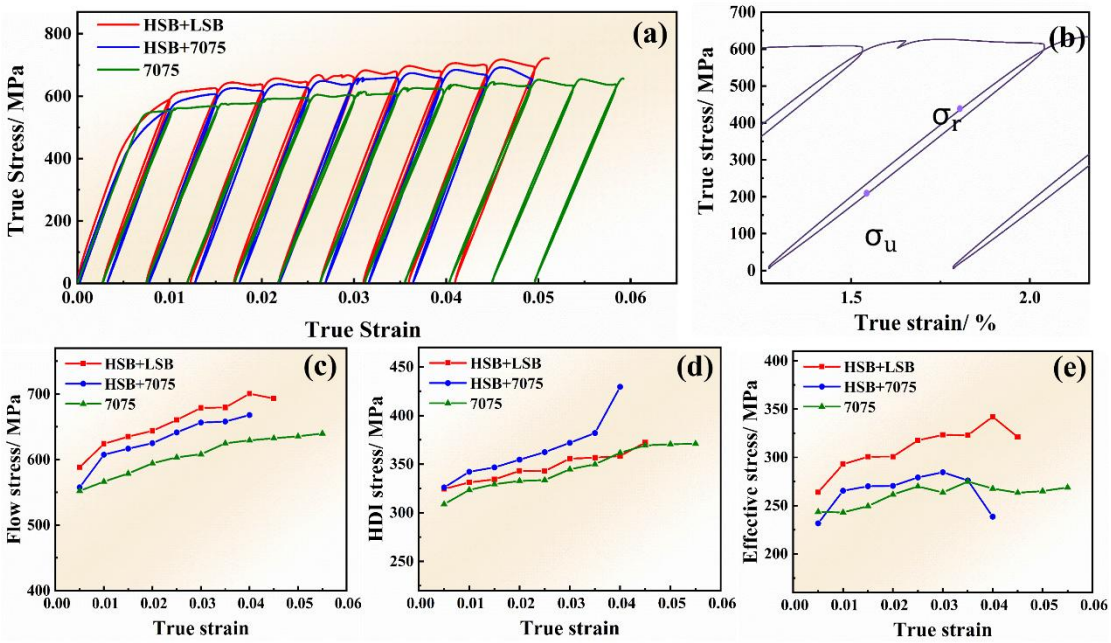


Fig. 10. (a) LUR stress-strain curve, (b) the unloading and reloading curve, (c) flow stress, (d) HDI stress and (e) effective stress at different true stain.

In addition to the intrinsic toughening arising from strain hardening, the extrinsic toughening mechanism governed by crack evolution also plays a critical role in dictating strength-ductility synergy. High-resolution CT reconstruction results (Fig. 11) reveal the spatial distribution of cracks near tensile fracture surfaces. Compared to HSB+LSB, HSB+7075 exhibits smaller average crack size and higher crack density in the necking region, as evidenced in Fig.11 (c, f). Such crack characteristics could lead to more uniform cracking and enhanced strain energy dissipation [33], which contributes to the improved El. The microcrack magnification diagram of HSB+LSB (Fig. 11(b)) presents a representative coarsened defect-coalescence, indicating a significant crack instable propagation during deformation. It could be understood that n-SiC introduced defect nucleation sites in the CG zones of HSB+LSB could accelerate the strain localization and microcrack propagation [38-40]. Fig.11 (g-i) display a higher crack

density and sphericity observed in 7075Al, which is the typical characteristic feature of ductile fracture.

Accordingly, although the modification strategy on CG zones by introducing nanodispersoids can enhance the YS, the synergistic improvement in strength-ductility is essentially a combined outcome of multiple factors, e.g., strain gradients, nanoprecipitates and crack evolutions. In other words, the superior comprehensive mechanical properties of HSB+7075 in the present study stem from the cooperative mechanism of intrinsic toughening induced by improved HDI strain hardening and extrinsic toughening governed by crack homogenization.

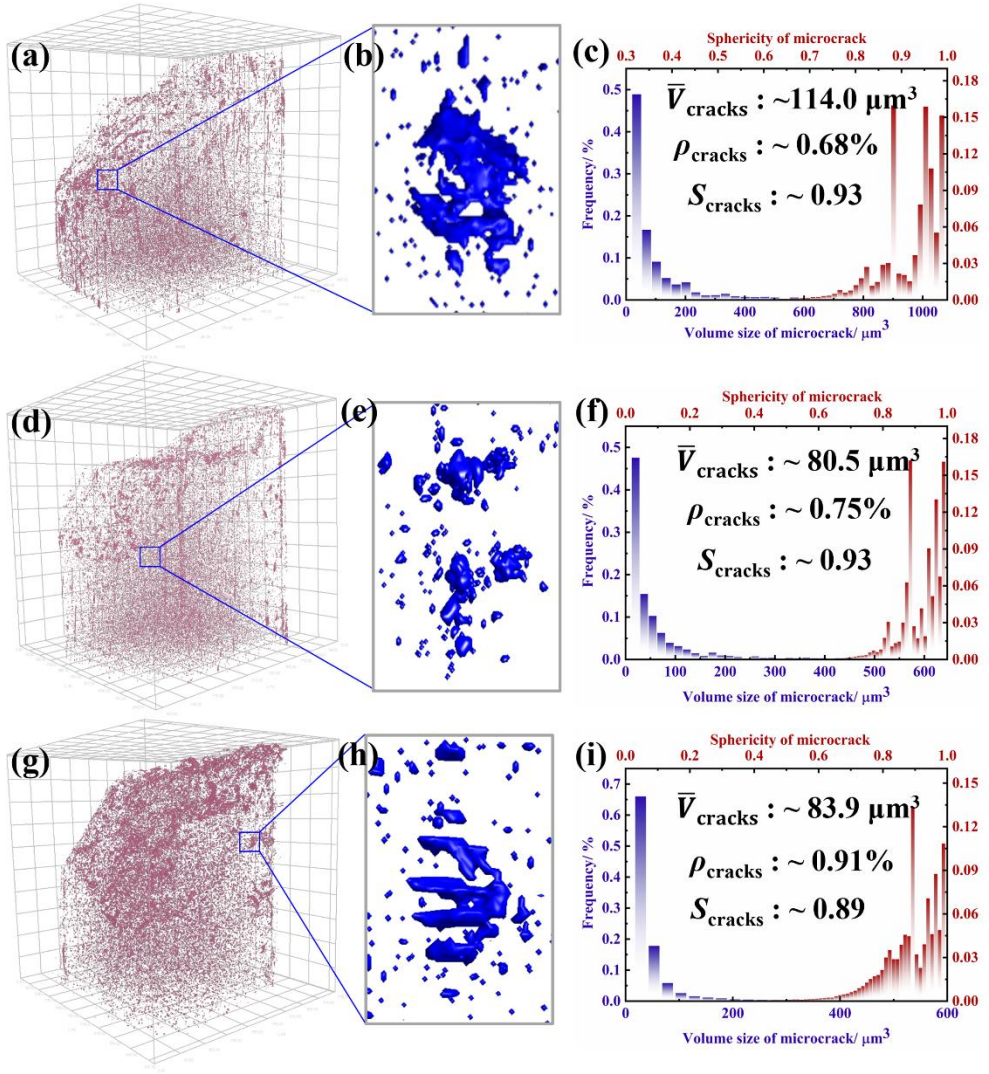


Fig. 11. High resolution-CT characterization for the microcrack feature in: (a, b) HSB+LSB, (d, e) HSB+7075, (g, h) 7075Al, statistical results for crack volume size ($\overline{V}_{cracks}$), crack volume density (ρ_{cracks}) and crack sphericity (S_{cracks}): (c) HSB+LSB, (f) HSB+7075, (i) 7075Al.

4.2 Unique aging precipitation behaviors in composites

TEM analysis reveals that the number densities of the η′ and η phases in 7075Al are higher than those of the GPII zones and η′ phase in the composites. This observation suggests that the aging kinetics in composites are quite different from that in 7075Al under identical aging conditions. This kinetic disparity is attributed to the altered migration and segregation behavior of Mg atoms, which play a critical role in controlling the aging process. The role of Mg evolves during the aging process: initially, its interaction with vacancies promotes the formation of cluster/GP zones, while later, its substitution for Al in the metastable η′ phase directly promotes the transformation to the stable η phase [2, 44, 45]. The extensive n-SiC/Al interfaces in the composites enhance Mg segregation (Fig. 5(a_1) and Fig. 6(e_3)), diverting Mg to form coarse GBPs such as Mg $(Zn, Cu, Al)_2$. This reduces the Mg content available for intragranular precipitation compared to the alloys, leading to a kinetic retardation of aging process within grains.

Moreover, the precipitation behavior in CG and UFG zones of the composites also exhibits significant differences (as shown in Fig. 5(c) and Fig. 6(c, e)). Owing to the high concentration of grain boundaries and n-SiC/Al interfaces in the UFG structure, which facilitates the diffusion and segregation of Mg, Zn solutes [46], the coarse equilibrium phases form a homogeneous distribution with negligible size variation between the grain interiors and boundaries. Hu et al. revealed the fundamental reasons for the low precipitation density within UFG materials [20]. On one hand, during quenching and subsequent aging processes, a substantial number of supersaturated vacancies migrate to grain boundaries and annihilate, resulting in a reduced actual vacancy concentration within the grain interiors. The lack of vacancies directly suppresses the homogeneous nucleation of GP zones, which relies on the formation of vacancy-solute clusters. On the other hand, grain refinement promotes the absorption of dislocations into grain boundaries, thereby decreasing the heterogeneous nucleation sites. The dual suppression of both homogeneous and heterogeneous nucleation mechanisms functioning in UFG zones ultimately leads to an exceptionally low intragranular precipitation density.

The localized segregation of solute elements migrating from CG to UFG zones,

induced by the short-circuit diffusion of UFG structure with high-density grain boundaries, is corroborated by the EDS mapping of composites, which is consistent with the observation that Mg and Zn signals in the CG zones are significantly weaker than those in UFG zones (Fig. 5(a_3) and Fig. 6(a_3)). Given the inherently low supersaturation that discourages homogeneous nucleation, the nanoprecipitates within the CGs of HSB+7075 exhibit lower density than those of 7075Al. Even more, the intragranular homogeneous precipitation in the CG zones of HSB+LSB is further suppressed and confined almost exclusively along the dislocations. This is attributed to the additional n-SiC/Al interfaces introduced by dispersive n-SiC, which facilitates the localized distribution of Mg and Zn and obstructs homogeneous nucleation. Fig. S1 provides clear evidence for the role of dislocation pipe diffusion in facilitating the growth of precipitates within both the composites and alloy [41]. The enhancement factor *f* enables quantitative analysis of the effect of dislocation pipe diffusion on precipitate size [26] :

$$f = 1 + \frac{b\sqrt{2}}{\pi R} \times \sqrt{f(t') \times \frac{\sqrt{D_p}}{\sqrt{D}}} \quad (3)$$

where b is the burgers vector, b=0.286 nm; *R* is the radius of precipitates, *R*=7.90 nm (7075Al); D_p is the diffusivity of the rate-limiting species (Zn) along the dislocation core, $D_{p=}10^{-17}$ m^2/s [26]; *D* is the bulk diffusivity of the rate-controlling solute species (Zn) at 120 ℃ aging temperature, D=7.4x10^{-22} m^2/s [41]; The function *f(t ´)* is an integral with respect to time t´. As the duration varies from 100 seconds to 1000 seconds, the integral value ranges from 0.85 to 0.62. During this research, *f(t ´)* was taken as 0.85 [26]. The final calculated value of the enhancement factor *f* is approximately 1.87. When considering the combined effects of bulk diffusion and pipe diffusion, the growth rate of the precipitates is 1.87 times that of the growth rate when only bulk diffusion is considered.

In summary, the precipitation behavior in composites is highly heterogeneous and governed by the distribution of n-SiC and the accompanying defects. The preferential segregation of Mg to n-SiC/Al interfaces and grain boundaries depletes the solute atoms, thereby suppressing the intragranular precipitation. On this basis, the formation of

nanoprecipitates in UFG interiors is further obstructed by the superposition of vacancy annihilation and dislocation absorption into boundaries. The n-SiC decorated CGs also suffers from the decrease of solute supersaturation, making intragranular nanoprecipitates prefer to form along dislocations rather than homogeneously. A reasonable explanation is given by pipe diffusion, which accelerates the growth of nanoprecipitates nucleated on dislocations, with an enhancement factor of approximately 1.87. These results demonstrate the intrinsic differences in precipitate density and distribution between composites and unreinforced 7075Al, arising from the competing effects of solute segregation, vacancy depletion and dislocation-assisted diffusion. The nanodispersoids introduced into CG zones are not isolated but accompanied by the evolutions of precipitation behavior.

4.3 Strengthening mechanisms of composites and alloys

The theoretical YS of composites is attributed to a combination of strengthening mechanisms, e.g., grain refinement, dislocation hardening, Orowan strengthening, HDI strengthening, and load transfer strengthening. To quantitatively deconvolute the contribution of each mechanism, the respective strengths were calculated using the following equations (the HDI strength value was obtained from the LUR test).

Grain boundaries serve as strong barriers that impede the long-range cross-grain dislocation propagation, leading to pile-ups and stress concentration. This strengthening mechanism can be quantitatively described by the Hall-Petch equation [49]:

$$\sigma_{GB} = \sigma_0 + k/\sqrt{d} \quad (4)$$

where σ_0 is the friction stress, σ_0=5 MPa [16], k is the Hall-Petch constant (k=0.12 MPa·m$^{1/2}$) [19], d is the average grain size (the value of d is derived from the EBSD results and is presented in Table. 2.) The contributions to grain boundary strengthening for 7075Al, HSB+7075, and HSB+LSB are 47 MPa, 119 MPa, and 100 MPa respectively. The contribution of UFG to strength is approximately 53~72 MPa.

The strengthening increment from dislocation interactions, including forest hardening resulting from the intersection and tangling of high-density dislocations, is

calculated via the Bailey-Hirsch relationship [50]:

$$\sigma_d = M\alpha G\mathrm{b}\rho^{1/2} \quad (5)$$

where M is the Mean orientation factor, M=3.06 for fcc matrix [48]; α is the constant, α=0.2 for fcc metals [47]; G is the shear modulus, G=26.9 GPa for 7075Al [19]; ρ is the dislocation density, The value of ρ is obtained by linear fitting the XRD results according to the William Hall method.

The strengthening contributions from the stable η phase in 7075Al and the n-SiC within the UFG of the composite are predominantly governed by the Orowan bypassing mechanism. In contrast, for the coherent/semi-coherent GP zones and η′ phase in the CG zone of the composite, as well as the remaining η′ phase in 7075Al, the dominant strengthening mechanism is determined by the lower value between the Orowan bypassing and the dislocation shearing mechanisms [19].

The contribution of UFG intragranular n-SiC to strength is calculated using Eq. (6) [51]:

$$\sigma_{n-SiC} = \frac{0.8MG\mathrm{b}}{2\pi\sqrt{1-\upsilon}} \cdot ln\frac{d_{n-SiC}/\mathrm{b}}{\lambda - d_{n-SiC}} \quad (6)$$

where υ is Possion's ration (υ=0.33 for 7075Al [19]); d_{n-SiC} is the average particle size of n-SiC; λ is the average spacing between n-SiC, $\lambda = \frac{1}{2}d_{n-SiC}(\frac{3\pi}{2f_{n-SiC}^{intra}})^{\frac{1}{2}}$, where f_{n-SiC}^{intra} is the local volume fraction of intragranular n-SiC. Fig. S2 shows detailed information on the distribution provides a detailed view of the distribution of n-SiC in the UFG zones. The σ_{n-SiC} values for both the HSB+7075 and HSB+LSB are 27 MPa and 29 MPa, respectively.

For plate-like η/η′ precipitates, their contribution to strength is calculated using the modified Orowan bypassing Eq. (7) [52]:

$$\sigma_{or} = \frac{MG\mathrm{b}}{2\pi\sqrt{1-\upsilon}}\ (1.123d_p \cdot \sqrt{\frac{0.318\pi}{af_p}} - \frac{\pi d_p}{8} - \frac{1.061d_p}{a})^{-1} \cdot \ln\ \frac{0.981d_p}{a\mathrm{b}} \quad (7)$$

where d_p is the average diameter of intragranular precipitates; f_p is the volume fraction of intragranular precipitates; a is the diameter to thickness ratio of intragranular precipitates.

The strength increment induced by the dislocation shearing mechanism comprises coherency strengthening (σ_{cs}), modulus mismatch strengthening (σ_{ms}) and order

strengthening (σ_{os}). The larger of σ_{cs} + σ_{ms} or σ_{os} is the total strength increment from the dislocation shearing mechanism [19]. The values of σ_{cs}, σ_{ms} and σ_{os} are calculated from Eq. (8) - (10), respectively [53-56].

$$\sigma_{cs} = M\alpha_{\varepsilon}(Ge_c)^{\frac{3}{2}}\left(\frac{rf_p}{0.5G\mathrm{b}}\right)^{\frac{1}{2}} \quad (8)$$

$$\sigma_{ms} = M0.0055(\Delta G)^{\frac{3}{2}}(\frac{2f_p}{G})^{\frac{1}{2}}(\frac{r}{\mathrm{b}})^{\frac{3\mathrm{m}}{2}-1} \quad (9)$$

$$\sigma_{os} = M0.81\frac{\gamma_{apb}}{2\mathrm{b}}\left(\frac{3\pi f_p}{8}\right)^{\frac{1}{2}} \quad (10)$$

where α_{ε} =2.6 for fcc metals; e_c is the constrained lattice parameter misfit, e_c≈ 0.03 for η′/7075Al, e_c≈ 0.06 for GP zone/7075Al; r is the mean radius of intragranular precipitates, r =0.5d_p; γ_{apb} is the antiphase boundary free energy of the precipitates; m=0.85; ΔG is the modulus mismatch between the matrix and the precipitates.

Substituting the parameters into Eq. (7), the calculated σ_{or} for 7075, HSB+7075, and HSB+LSB are 174 MPa, 36 MPa, and 28 MPa respectively. The σ_{cs} for the η′ phase and GP zone, calculated from Eq. (8), are 576 MPa and 1880 MPa respectively. Since $\sigma_{or} < \sigma_{cs}$, Orowan bypassing strengthening is the dominant strengthening mechanism in η′ phase and GP zone.

The underlying mechanism of load transfer is the efficient redistribution of stress from 7075Al matrix to n-SiC during deformation. It is noteworthy that employing n-SiC maximizes the interfacial area, promoting a homogeneous stress distribution and superior load-bearing efficiency. The load transfer effect σ_{l-t} could be estimated by Eq. (11) [57]

$$\sigma_{l-t} = \frac{1}{2}\tau_m VS \quad (11)$$

where τ_m is the Shear YS of 7075Al, (τ_m=$\sigma_m/\sqrt{3}$, σ_m=532.72 MPa); V is the volume fraction of n-SiC; S is the aspect ratio of n-SiC (S=1). The σ_{l-t} values for the HSB+7075 and HSB+LSB are 12 MPa and 13 MPa respectively.

As detailed in Table 4, the calculated theoretical values indicate that 7075Al, as one of the well-established precipitation hardened series, is primarily enhanced through Orowan strengthening by nanoprecipitates, which contributes approximately 174 MPa in YS. The introduction of high-content unshearable n-SiC contributes about 30 MPa

to the YS of composites through dislocation bypassing mechanism, but also leads to the recession of intragranular precipitation behaviors, as discussed in section 4.2. Given the density of precipitates in CG and UFG zones of HSB+7075 and HSB+LSB is extremely low, the corresponding contributions from precipitation hardening are only 36 MPa and 28 MPa, respectively. The reinforcement of composites primarily relies on HDI strengthening, contributing approximately 325 MPa of YS according to LUR experimental results. Fig. 12(a, b) show the comparative scatter diagrams focusing on El & UTS and El & σ_b-$\sigma_{0.2}$, respectively, for the composites prepared in this work and recently reported Al-Zn-Mg-Cu based composites. It can be seen that HSB+LSB and HSB+7075 demonstrate a well-balanced strength-ductility and an improved strain hardening efficiency ($\frac{\sigma_b-\sigma_{0.2}}{\varepsilon}$).

Table 4. Theoretical yield strength increments of 7075Al and n-SiC/7075Al composites from different strengthening mechanisms.

Sample	σ_{GB}/MPa	σ_d/MPa	σ_{Orowan}/MPa	σ_{l-t}/MPa	σ_{HDI}/MPa	σ_{th}/MPa	σ_{ex}/MPa
HSB+LSB	100	98	28+29	13	325	593	547.87
HSB+7075	119	103	36+27	12	326	623	538.40
7075	47	90	174	/	308	619	532.72

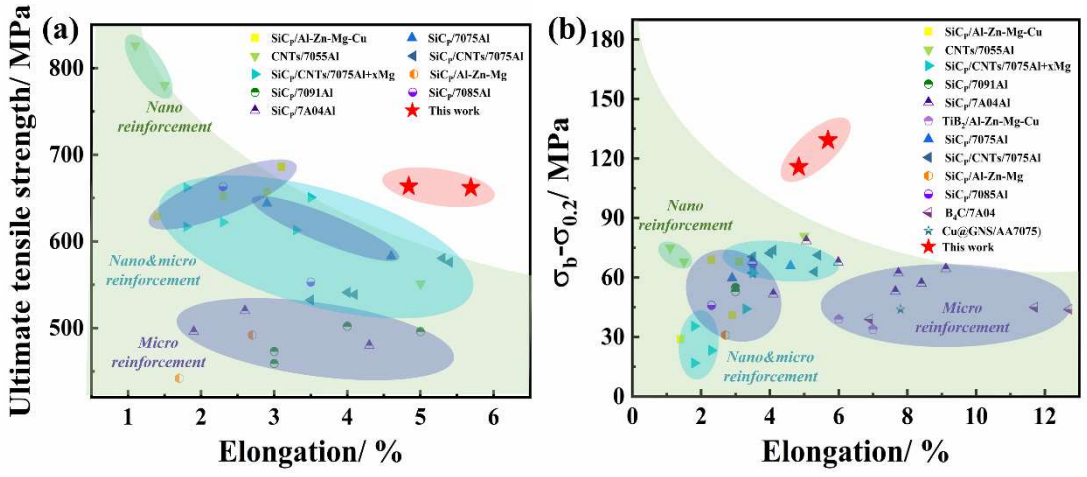


Fig. 12. Tensile properties comparison of this work with other Al matrix composites: (a) comparison chart of UTS, (b) comparison chart of σ_b-$\sigma_{0.2}$ [10] [12] [13] [15] [58-75].

5. Conclusions

Heterogeneous bimodal-grained 7075Al matrix composites incorporating high-content (≥7.5 wt%) locally distributed n-SiC were fabricated via powder metallurgy. The effect of microstructural characteristics of CG zones on mechanical responses was investigated. Samples whose CG components evolved from 7075Al powders uniformly embedded with n-SiC are denoted as HSB+LSB, while those containing unmodified 7075Al powders are denoted as HSB+7075. The conclusions are as follows:

(1) Unlike 7075Al, both HSB+LSB and HSB+7075 exhibit a two-stage yielding and remarkably enhanced strain hardening efficiency. Compared with HSB+LSB, HSB+7075 shows comparable YS (538.4 MPa) and UTS (662.0 MPa), yet delivers a 20% increase in El (5.7%) and an improved strain hardening exponent (0.078), thereby achieving an excellent strength-ductility synergy.

(2) Precipitation in composites is dominated by the locally distributed n-SiC and the associated defects. The difference in precipitating behaviors between HSB+7075 and HSB+LSB originates from CG zones, i.e., nanoprecipitates tend to be homogeneously distributed in the former, but nucleate via pipe diffusion and grow along dislocations in the latter, due to the n-SiC/Al interface induced solute segregation.

(3) The high-content n-SiC induced degradation of intragranular nanoprecipitates reduces the strengthening contribution from Orowan mechanism by approximately 110 MPa, compared with that of 7075Al. As a result, the strengthening of HSB+7075 and HSB+LSB is instead dominated by HDI mechanism, which contributes over 325 MPa to the YS.

(4) The superior ductility of HSB+7075 derives from the combination between intrinsic toughening promoted by improved HDI strain hardening capacity, and extrinsic toughening governed by cracking delocalization. Such a synergy results from the coupled effects of multiple factors, e.g., strain gradients, nanoprecipitates and microcrack evolutions.

Acknowledgement

This work was financially supported by National Key Research and Development Program of China (No. 2023YFB4606200) and National Natural Science Foundation of China (No. 52601295, 52471161, 52192595), China Postdoctoral Science Foundation (No. 2026M790110) and Shanghai Jiao Tong University 2030 Initiative.

References

[1] Azarniya A, Taheri A K, Taheri K K. Recent advances in ageing of 7xxx series aluminum alloys: A physical metallurgy perspective. J Alloys Compd, 2019, 781: 945-983.

[2] Berg L K, Gjønnes J, Hansen V, et al. GP-zones in Al–Zn–Mg alloys and their role in artificial aging. Acta Mater, 2001, 49: 3443-3451.

[3] Yang W, Ji S, Wang M, et al. Precipitation behaviour of Al–Zn–Mg–Cu alloy and diffraction analysis from η′ precipitates in four variants. J Alloys Compd, 2014, 610: 623-629.

[4] Sha G, Cerezo A. Early-stage precipitation in Al–Zn–Mg–Cu alloy (7050). Acta Mater, 2004, 52: 4503-4516.

[5] Williams JC, Starke EA. Progress in structural materials for aerospace systems. Acta Mater, 2003, 51: 5775–99.

[6] Liddicoat P V, Liao X Z, Zhao Y, et al. Nanostructural hierarchy increases the strength of aluminium alloys. Nat. Commun., 2010, 1: 63.

[7] Shen Q, Wu C, Luo G, et al. Microstructure and mechanical properties of Al-7075/B_4C composites fabricated by plasma activated sintering. J Alloys Compd, 2014, 588: 265-270.

[8] Yang Q, Cheng D L, Zhang F G, et al. Spark plasma sintering mechanisms of the Al-Zn-Mg-Cu alloys and TiB_2/Al-Zn-Mg-Cu composites. Mater Charact, 2021, 172: 110825.

[9] Zhang Z, Li Z, Tan Z, et al. Bioinspired hierarchical Al_2O_3/Al laminated composite fabricated by flake powder metallurgy. Compos Part A-Appl Sci Manufact, 2021, 140: 106187.

[10] Ma G N, Wang D, Liu Z Y, et al. An investigation on particle weakening in T6-treated SiC/Al–Zn–Mg–Cu composites. Mater Charact, 2019, 158: 109966.

[11] Wang X, Wang X, Liu K, et al. Effect of the CNTs into SiCp-Al interfacial micro-zones on ageing precipitation behavior, microstructure and mechanical properties of SiCp(CNT)/Al–Zn–Mg–Cu composites. Compos Part B-Eng, 2023, 259: 110708.

[12] Bi S, Liu Z Y, Xiao B L, et al. Different fatigue behavior between tension-tension and tension-compression of carbon nanotubes reinforced 7055 Al composite with bimodal structure. Carbon, 2021, 184: 364-374.

[13] Ma K, Liu Z, Zhang X, et al. Fabrication of high strength carbon nanotube/7055Al composite by powder metallurgy combined with subsequent hot extrusion. Sci. China Technol. Sci., 2021, 64: 1081-1091.

[14] Mohammed S M A K, Chen D L, Liu Z Y, et al. Deformation behavior and strengthening mechanisms in a CNT-reinforced bimodal-grained aluminum matrix nanocomposite. Mater Sci Eng-A, 2021, 817: 141370.

[15] Liu J, Liu C, Cai H, et al. Enhanced precipitate strengthening in particulates reinforced Al–Zn–Mg–Cu composites via bimodal structure design and optimum aging strategy. Compos Part B-Eng, 2023, 260: 110772.

[16] Guan L, Cao H, Su Y, et al. Enhanced strength–ductility synergy of SiC particles reinforced aluminum matrix composite via dual configuration design of reinforcement and matrix. Mater Des, 2024, 245: 113186.

[17] Liu K, Cui Q, Shi L, et al. Grain structure tailoring strategy for heterogeneous lamella SiC_p/2024Al composites with exceptional strength-ductility synergy. Compos Part B-Eng, 2024, 280: 111491.

[18] Zhao Y H, Liao X Z, Jin Z, et al. Microstructures and mechanical properties of ultrafine grained 7075Al alloy processed by ECAP and their evolutions during annealing. Acta Mater, 2004, 52: 4589-4599.

[19] Ma K, Wen H, Hu T, et al. Mechanical behavior and strengthening mechanisms in ultrafine grain precipitation-strengthened aluminum alloy. Acta Mater, 2014, 62: 141-155.

[20] Hu T, Ma K, Topping T D, et al. Precipitation phenomena in an ultrafine-grained Al alloy. Acta Mater, 2013, 61: 2163-2178.

[21] Jiang B, Zheng L, Xi C, et al. Microstructure and mechanical properties of TiB_2-reinforced 7075 aluminum matrix composites fabricated by laser melting deposition. Ceram. Int., 2019, 45: 5680-5692.

[22] Liu K, Su Y, Wang X, et al. Achieving simultaneous enhancement of strength and

ductility in Al matrix composites by employing the synergetic strengthening effect of micro- and nano-SiC_{ps}. Compos Part B-Eng, 2023, 248: 110350.

[23] Cao F, Zheng J, Jiang Y, et al. Experimental and DFT characterization of η′ nano-phase and its interfaces in Al Zn Mg Cu alloys. Acta Mater, 2019, 164: 207-219.

[24] Chung T F, Yang Y L, Huang B M, et al. Transmission electron microscopy investigation of separated nucleation and in-situ nucleation in AA7050 aluminium alloy. Acta Mater, 2018, 149: 377-387.

[25] Chung T F, Yang Y L, Shiojiri M, et al. An atomic scale structural investigation of nanometre-sized η precipitates in the 7050 aluminium alloy. Acta Mater, 2019, 174: 351-368.

[26] Deschamps A, Fribourg G, Bréchet Y, et al. In situ evaluation of dynamic precipitation during plastic straining of an Al–Zn–Mg–Cu alloy. Acta Mater, 2012, 60: 1905-1916.

[27] Dumont M, Lefebvre W, Doisneau-Cottignies B, et al. Characterisation of the composition and volume fraction of η′ and η precipitates in an Al–Zn–Mg alloy by a combination of atom probe, small-angle X-ray scattering and transmission electron microscopy. Acta Mater, 2005, 53: 2881-2892.

[28] Marlaud T, Deschamps A, Bley F, et al. Evolution of precipitate microstructures during the retrogression and re-ageing heat treatment of an Al–Zn–Mg–Cu alloy. Acta Mater, 2010, 58: 4814-4826.

[29] Marlaud T, Deschamps A, Bley F, et al. Influence of alloy composition and heat treatment on precipitate composition in Al–Zn–Mg–Cu alloys. Acta Mater, 2010, 58: 248-260.

[30] Sha G, Wang Y B, Liao X Z, et al. Influence of equal-channel angular pressing on precipitation in an Al–Zn–Mg–Cu alloy. Acta Mater, 2009, 57: 3123-3132.

[31] Luo J, Luo H, Li S, et al. Effect of pre-ageing treatment on second nucleating of GPII zones and precipitation kinetics in an ultrafine grained 7075 aluminum alloy. Mater Des, 2020, 187: 108402.

[32] Ma Y, Addad A, Ji G, et al. Atomic-scale investigation of the interface precipitation in a TiB_2 nanoparticles reinforced Al–Zn–Mg–Cu matrix composite. Acta Mater,

2020, 185: 287-299.

[33] Liu K, Cui Q F, Shi L, et al. Tuning lamella spacings for simultaneous strength-ductility improvements in heterogeneous lamella SiC_p/2024Al composites. Mater Des, 2025, 248: 113510.

[34] Guan L, Liu K, Huang B, et al. Governing high-content nanoparticles distribution for architecting high-performance bamboo-structured 2024Al matrix composites. Mater Res Lett, 2025, 13: 829-836.

[35] Wu X, Yang M, Yuan F, et al. Heterogeneous lamella structure unites ultrafine-grain strength with coarse-grain ductility. Proc Natl Acad Sci USA, 2015, 112: 14501-14505.

[36] Zhu Y, Wu X. Heterostructured materials. Prog. Mater. Sci., 2023, 131: 101019.

[37] Liu D, Wang J, Wang C, et al. Hetero-deformation-induced (HDI) plasticity induces simultaneous increase in both yield strength and ductility in a Fe50Mn30Co10Cr10 high-entropy alloy. Appl. Phys. Lett., 2021, 119: 131906.

[38] Fu X, Tan Z, Ma Z, et al. Powder assembly & alloying to CNT/Al–Cu–Mg composites with trimodal grain structure and strength-ductility synergy. Compos Part B-Eng, 2021, 225: 109271.

[39] Guo Z, Wang K, Cui B, et al. Ultrastrong and ductile Al–Mg alloy matrix composites via composition-modulated precipitation induced by intragranular ceramic nanoparticles. Compos Part B-Eng, 2025, 291: 112012.

[40] Guo Z, Li X, Wang S, et al. Prolonged work hardening in bimodal grain structured aluminum matrix composites: a sequential heterostructure effect. Int J Plast, 2025, 194: 104485.

[41] Ma K, Hu T, Yang H, et al. Coupling of dislocations and precipitates: Impact on the mechanical behavior of ultrafine grained Al–Zn–Mg alloys. Acta Mater, 2016, 103: 153-164.

[42] Li P Y, Li X N, Liu Z Y, et al. Enhanced strength–ductility synergy of carbon nanotube/Al–Cu–Mg composites via introducing laminate structure and grain modification. Compos Part B-Eng, 2022, 243: 110178.

[43] Yang M, Yan D, Yuan F, et al. Dynamically reinforced heterogeneous grain

structure prolongs ductility in a medium-entropy alloy with gigapascal yield strength. Proc Natl Acad Sci USA, 2018, 115: 7224-7229.

[44] Jiang H, Xing H, Xu Z, et al. Effect of pre-aging and precipitation behavior on mechanical properties of 7055 aluminum alloy processed by hot-forming quenching. Mater Charact, 2023, 198: 112729.

[45] Liu J Z, Chen J H, Yang X B, et al. Revisiting the precipitation sequence in Al–Zn–Mg-based alloys by high-resolution transmission electron microscopy. Scr. Mater., 2010, 63: 1061-1064.

[46] Christian J W. Precipitation from Supersaturated Solid Solution. The Theory of Transformations in Metals and Alloys. Elsevier, 2002: 718-796.

[47] Stoller R E, Zinkle S J. On the relationship between uniaxial yield strength and resolved shear stress in polycrystalline materials. J. Nucl. Mater., 2000, 283-287: 349-352.

[48] Courtney T H. Mechanical behavior of materials. Waveland Press, 2005.

[49] Pande C S, Cooper K P. Nanomechanics of Hall–Petch relationship in nanocrystalline material. Prog. Mater. Sci., 2009, 54: 689-706.

[50] Gao H, Huang Y, Nix W D, et al. Mechanism-based strain gradient plasticity— I. Theory. J. Mech. Phys. Solids, 1999, 47: 1239-1263.

[51] Aikin R M, Christodoulou L. The role of equiaxed particles on the yield stress of composites. Scr. Mater., 1991, 25: 9-14.

[52] Nie J F, Muddle B C. Strengthening of an Al–Cu–Sn alloy by deformation-resistant precipitate plates. Acta Mater, 2008, 56: 3490-3501.

[53] Wen H, Topping T D, Isheim D, et al. Strengthening mechanisms in a high-strength bulk nanostructured Cu–Zn–Al alloy processed via cryomilling and spark plasma sintering. Acta Mater, 2013, 61: 2769-2782.

[54] Booth-Morrison C, Dunand D C, Seidman D N. Coarsening resistance at 400 °C of precipitation-strengthened Al–Zr–Sc–Er alloys. Acta Mater, 2011, 59: 7029-7042.

[55] Seidman D N, Marquis E A, Dunand D C. Precipitation strengthening at ambient and elevated temperatures of heat-treatable Al(Sc) alloys. Acta Mater, 2002, 50:

4021-4035.

[56] Ardell A J. Precipitation hardening. Metall. Mater. Trans., 1985, 16: 2131-2165.

[57] Ryu H J, Cha S I, Hong S H. Generalized shear-lag model for load transfer in SiC/Al metal-matrix composites. J. Mater. Res., 2003, 18: 2851-2858.

[58] Lu T, Chen W, Xu W, et al. The effects of Cr particles addition on the aging behavior and mechanical properties of SiC_p/7075Al composites. Mater Charact, 2018, 136: 264-271.

[59] Chen Y T, Zhu S Z, Wang D S, et al. Reducing Mg segregation by solution temperature control to improve strength in SiC/7xxxAl composites. Ceram. Int., 2025, 51: 13797-13802.

[60] Ravi Kumar N V, Dwarakadasa E S. Effect of matrix strength on the mechanical properties of Al–Zn–Mg/SiC_P composites. Compos Part A-Appl Sci Manufact, 2000, 31: 1139-1145.

[61] Xiu Z, Yang W, Dong R, et al. Microstructure and Mechanical Properties of 45 vol.% SiC_p/7075Al Composite. J. Mater. Sci. Technol., 2015, 31: 930-934.

[62] Chen Y T, Zhu S Z, Luo H J, et al. Effects of solution temperatures on microstructures and mechanical properties of B_4C/7A04Al composites: A comparison study with 7A04Al alloys. Mater Sci Eng-A, 2024, 890: 145899.

[63] Rong X, Li Y, Chen X, et al. Achieving high mechanical properties and corrosion resistance of Al-Zn-Mg matrix composites via regulating intragranular reinforcements. J. Mater. Sci. Technol., 2023, 153: 1-7.

[64] Chen W, Liu Y, Yang C, et al. (SiCp+Ti)/7075Al hybrid composites with high strength and large plasticity fabricated by squeeze casting. Mater Sci Eng-A, 2014, 609: 250-254.

[65] Lu T W, Chen W P, Wang P, et al. Enhanced mechanical properties and thermo-physical properties of 7075Al hybrid composites reinforced by the mixture of Cr particles and SiC_p. J Alloys Compd, 2018, 735: 1137-1144.

[66] Zhao S, Zhang H, Cui Z, et al. Strength and ductility improvement of an in-situ TiB_2/Al–Zn–Mg–Cu composite by elliptical cross-section torsion extrusion. Compos Part B-Eng, 2021, 216: 108843.

[67] Liu Y X, Zheng Z X, Zhu D Z, et al. Effects of heat treatment on microstructure and mechanical properties of SiCp/7075Al composites. Trans. Mater. Heat Treat., 2018, 39: 1-6.

[68] Zhao K, Han G, Gao T, et al. Interface precipitation and corrosion mechanisms in a model Al–Zn–Mg–Cu alloy strengthened by TiC particles. Corros. Sci., 2022, 206: 110533.

[69] Ma G, Wang D, Xiao B, et al. Effect of Particle Size on Mechanical Properties and Fracture Behaviors of Age-Hardening SiC/Al–Zn–Mg–Cu Composites. ACTA METALL. SIN., 2021, 34: 1447-1459.

[70] Manoharan M, Lewandowski J J. Effect of reinforcement size and matrix microstructure on the fracture properties of an aluminum metal matrix composite. Mater Sci Eng-A, 1992, 150: 179-186.

[71] Zhao W, Liu R feng, Yan J, et al. Overall optimization in microstructure and mechanical properties of 5 wt% SiC/7075Al composites by high-frequency electric pulse assisted treatment. J. Mater. Res. Technol., 2022, 21: 2156-2167.

[72] Wang X, Wang S, Wang X, et al. Synergistic strengthening-toughening effect of SiC_p(CNT) hybrid reinforcements on Mg-compensated SiC_p(CNT)/Al–Zn–Mg–Cu composites. Mater Sci Eng-A, 2024, 892: 145999.

[73] Lu T, Scudino S, Chen W, et al. The influence of nanocrystalline CoNiFeAl0.4Ti0.6Cr0.5 high-entropy alloy particles addition on microstructure and mechanical properties of SiC_p/7075Al composites. Mater Sci Eng-A, 2018, 726: 126-136.

[74] Al-Furjan M S H, Hajmohammad M H, Shen X, et al. Evaluation of tensile strength and elastic modulus of 7075-T6 aluminum alloy by adding SiC reinforcing particles using vortex casting method. J Alloys Compd, 2021, 886: 161261.

[75] Song J, Guo Q, Ouyang Q, et al. Influence of interfaces on the mechanical behavior of SiC particulate-reinforced Al–Zn–Mg–Cu composites. Mater Sci Eng-A, 2015, 644: 79-84.

Supplementary Files

This is a list of supplementary files associated with this preprint. Click to download.

- file.docx